ROBUST TRACKING CONTROL OF A MAGNETICALLY SUSPENDED RIGID BODY

Kyong B. Lim* and David E. Cox†
NASA Langley Research Center
Hampton, Virginia

SUMMARY

This study is an application of H_∞ and μ-synthesis for designing robust tracking controllers for the Large Angle Magnetic Suspension Test Facility (LAMSTF). The modeling, design, analysis, simulation and testing of a control law that guarantees tracking performance under external disturbances and model uncertainties is investigated. The type of uncertainties considered and the tracking performance metric used is discussed. This study demonstrates the tradeoff between tracking performance at low frequencies and robustness at high frequencies. Two sets of controllers were designed and tested. The first set emphasized performance over robustness while the second set traded off performance for robustness. Comparisons of simulation and test results are also included. Current simulation and experimental results indicate that reasonably good robust tracking performance can be attained for this system using a multivariable robust control approach.

1 Introduction

The Large Angle Magnetic Suspension Test Facility (LAMSTF) has been assembled by NASA Langley Research Center for inhouse research in magnetic suspension technology. Reference [1] and the references therein give a detailed description of the facility and discuss in detail the open-loop dynamic properties of the magnetic suspension system. This system represents a scaled model of a planned Large-Gap Magnetic Suspension System (LGMSS). Robust tracking control for the LAMSTF consists of controlling the attitude and position of the suspended rigid body in the presence of external disturbances and model uncertainties. The motion of the suspended rigid body is in general nonlinear and hence the linear, time-invariant perturbed motion about an equilibrium state is considered in this study.

The underlying assumption in this study is that sufficiently accurate nominal and uncertainty models can be obtained from first principles combined with laboratory experiments. Indeed, currently there is a great deal of interest in the robust control community involving system identification for robust control. This motivates designing controllers that are robust to modeled uncertainties. We note that although empirical models could be synthesized through extensive testing in the laboratory or even in space, there are always physical limitations on the accuracy of the empirical model. The novelty in this paper consists in defining robust tracking performance, modeling of uncertainties, and evaluating simulation and experimental results.

The work reported herein parallels references [2]-[6]. The study reported in [2]-[6] considers vibration attenuation and fine-pointing control for a stable large flexible laboratory structure. In stark contrast to the above passively stable flexible structure, the LAMSTF system considered is a highly unstable rigid body. Furthermore, the nature of the uncertainties in the two systems differ; the uncertainty in the system in [2]-[6] is mostly due to inaccurate knowledge of damping, frequency and modeshapes of the structural modes and truncated higher frequency structural modes while for LAMSTF, the uncertainty is mostly due to errors

*Research Engineer, Spacecraft Controls Branch, Guidance and Control Division.
†Research Engineer, Spacecraft Controls Branch, Guidance and Control Division.

in the linearization about the equilibrium state, an inaccurate knowledge of the spatial distribution of the magnetic field, errors in the sensor system hardware, and errors at the plant input due to induced eddy currents.

2 LAMSTF Model

The system shown in Fig.1 is the LAMSTF system located at NASA Langley Research Center. This system basically consists of five electromagnets which actively suspend a small cylindrical permanent magnet. The cylinder is a rigid body and has six independent degrees of freedom, namely, three displacements and three rotations.

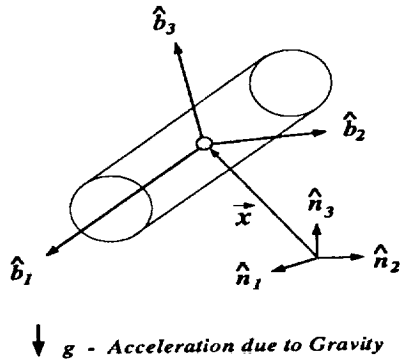

Figure 1: LAMSTF Configuration

2.1 Nonlinear Model

Let the unit vectors, $\hat{b}_i$ and $\hat{n}_i$, denote the i-th components of body and inertial coordinates which are initially assumed to be colinear. Define the following variables: the angular velocity of cylinder with respect to inertial frame $\vec{\omega} = \sum_{i=1}^{3} \omega_i \hat{b}_i$, disturbance torque about centroid $\vec{\Gamma} = \sum_{i=1}^{3} \Gamma_i \hat{b}_i$, centroid velocity $\vec{v} = \sum_{i=1}^{3} v_i \hat{n}_i$, position of centroid relative to origin of inertial frame $\vec{x} = \sum_{i=1}^{3} x_i \hat{n}_i$, and disturbance force acting on cylinder excluding magnetic forces as $\vec{F}_{ex} = \sum_{i=1}^{3} F_i \hat{n}_i$. Let $(\beta_0, \beta_1, \beta_2, \beta_3)$ denote the Euler parameters [7] which describe the attitude of the cylinder. The Euler parameters satisfy

$$\sum_{i=0}^{3} \beta_i = 1 \tag{1}$$

and the general rotational motion can be viewed as motions on the surface of a unit four dimensional hypersphere. Denote the direction cosine matrix by $C_{ij}, i, j = [1, 2, 3]$ where $\hat{b} = C\hat{n}$. The direction cosines are related to the Euler parameters by

$$C = \begin{bmatrix} \beta_0^2 + \beta_1^2 - \beta_2^2 - \beta_3^2 & 2(\beta_1\beta_2 + \beta_0\beta_3) & 2(\beta_1\beta_3 - \beta_0\beta_2) \\ 2(\beta_1\beta_2 - \beta_0\beta_3) & \beta_0^2 - \beta_1^2 + \beta_2^2 - \beta_3^2 & 2(\beta_2\beta_3 + \beta_0\beta_1) \\ 2(\beta_1\beta_3 + \beta_0\beta_2) & 2(\beta_2\beta_3 - \beta_0\beta_1) & \beta_0^2 - \beta_1^2 - \beta_2^2 + \beta_3^2 \end{bmatrix} \tag{2}$$

Due to symmetry about the 1-axis, the mass moment of inertia about the body axis is denoted by I_1 and $I_2 = I_3 = I_c$. Let the physical parameters, ν, M_x, and m_c, denote the core volume, core magnetization, and mass of the suspended body, respectively. The nonlinear equation of motion for the cylindrical magnet in a magnetic field is given as follows:

$$\begin{Bmatrix} \dot{\omega}_1 \\ \dot{\omega}_2 \\ \dot{\omega}_3 \end{Bmatrix} = -\begin{Bmatrix} 0 \\ \frac{I_1 - I_c}{I_c}\omega_1\omega_3 \\ \frac{I_c - I_1}{I_c}\omega_1\omega_2 \end{Bmatrix} + \frac{\nu M_x}{I_c}\begin{Bmatrix} 0 \\ -C_{31}B_1 - C_{32}B_2 - C_{33}B_3 \\ C_{21}B_1 + C_{22}B_2 + C_{23}B_3 \end{Bmatrix} + \begin{Bmatrix} \Gamma_1/I_1 \\ \Gamma_2/I_c \\ \Gamma_3/I_c \end{Bmatrix} \tag{3}$$

$$\begin{Bmatrix} \dot{\beta}_0 \\ \dot{\beta}_1 \\ \dot{\beta}_2 \\ \dot{\beta}_3 \end{Bmatrix} = \frac{1}{2}\begin{bmatrix} 0 & -\omega_1 & -\omega_2 & -\omega_3 \\ \omega_1 & 0 & \omega_3 & -\omega_2 \\ \omega_2 & -\omega_3 & 0 & \omega_1 \\ \omega_3 & \omega_2 & -\omega_1 & 0 \end{bmatrix}\begin{Bmatrix} \beta_0 \\ \beta_1 \\ \beta_2 \\ \beta_3 \end{Bmatrix} \tag{4}$$

$$\begin{Bmatrix} \dot{v}_1 \\ \dot{v}_2 \\ \dot{v}_3 \end{Bmatrix} = \frac{\nu M_x}{m_c}\begin{bmatrix} B_{11} & B_{12} & B_{13} \\ B_{21} & B_{22} & B_{23} \\ B_{31} & B_{32} & B_{33} \end{bmatrix}\begin{Bmatrix} C_{11} \\ C_{12} \\ C_{13} \end{Bmatrix} - \begin{Bmatrix} 0 \\ 0 \\ g \end{Bmatrix} + \frac{1}{m_c}\begin{Bmatrix} F_1 \\ F_2 \\ F_3 \end{Bmatrix} \tag{5}$$

$$\begin{Bmatrix} \dot{x}_1 \\ \dot{x}_2 \\ \dot{x}_3 \end{Bmatrix} = \begin{Bmatrix} v_1 \\ v_2 \\ v_3 \end{Bmatrix} \tag{6}$$

The variables, B_i and B_{ij}, denote the i-th inertial component of the magnetic field and its gradient in the j-th inertial direction at the instantaneous centroid location of the suspended magnet, respectively. Hence, in general, $B_i = B_i(x, \rho)$, and $B_{ij} = B_{ij}(x, \rho)$ are dependent on the instantaneous centroid location of the suspended mass, $x = (x_1, x_2, x_3)^T$, and the current applied to the five electromagnets, $\rho = (\rho_1, \ldots, \rho_5)^T$.

By defining the (13 by 1) state vector

$$\eta = (\omega_1, \omega_2, \omega_3,\ \beta_0, \beta_1, \beta_2, \beta_3,\ v_1, v_2, v_3,\ x_1, x_2, x_3)^T \tag{7}$$

and external disturbances

$$q = (\ \Gamma_1/I_1 \quad \Gamma_2/I_c \quad \Gamma_3/I_c \quad O_{1\times 4} \quad F_1/m_c \quad F_2/m_c \quad F_3/m_c \quad O_{1\times 3}\ )^T \tag{8}$$

the equation of motion can be written as

$$\dot{\eta} = f(\eta, \rho) + q \tag{9}$$

The five currents are the only control variables.

Currently, the general analytical expressions for $B_i(x, \rho)$ and $B_{ij}(x, \rho)$ are not available. However, the magnetic field is approximated quadratically in a small neighborhood around a nominal position and current, (x_o, ρ_o). Indeed, based on empirical measurements from the laboratory and with the aid of computer modeling, numerical values for the field distribution, its gradient, and curvature have been obtained about a point which is conveniently chosen to be the origin of the inertial coordinates. Let $x = x_o + \delta x$ and $\rho = \rho_o + \delta\rho$ denote the instantaneous centroid positions and the coil currents respectively. Then the measured second-order description of the i-th field component about the nominal values are given by

$$\begin{aligned} B_i(x, \rho) &= B_i(x_o, \rho_o) + \left[\frac{\partial B_i}{\partial(x_o, \rho_o)}\right]\begin{Bmatrix} \delta x \\ \delta\rho \end{Bmatrix} \\ &+ \frac{1}{2}\begin{Bmatrix} \delta x \\ \delta\rho \end{Bmatrix}^T\left[\frac{\partial^2 B_i}{\partial(x_o, \rho_o)^2}\right]\begin{Bmatrix} \delta x \\ \delta\rho \end{Bmatrix} + \text{ Higher Order Terms} \end{aligned} \tag{10}$$

The field gradients are also approximated by the quadratic fields, i.e., linearly approximated.

2.2 Equilibrium State

For convenience, the nominal position and currents are chosen at an equilibrium state. Consider the candidate equilibrium state

$$\eta_o = (0,0,0,\ \ 1,0,0,0,\ \ 0,0,0,\ \ 0,0,0)^T \tag{11}$$

This equilibrium state corresponds to the body frame being colinear with inertial frame with zero angular and translational velocities. Imposing the requirement, $\dot{\eta} = 0$ at state η_o for zero external disturbances, leads to the equilibrating field and gradients which satisfy

$$\begin{bmatrix} C_{21} & C_{22} & C_{23} \\ C_{31} & C_{32} & C_{33} \end{bmatrix}_{\eta_o}\begin{Bmatrix} B_1 \\ B_2 \\ B_3 \end{Bmatrix}_{\eta_o} = \begin{Bmatrix} 0 \\ 0 \end{Bmatrix} \tag{12}$$

$$\frac{\nu M_x}{m_c}\begin{bmatrix} B_{11} & B_{12} & B_{13} \\ B_{21} & B_{22} & B_{23} \\ B_{31} & B_{32} & B_{33} \end{bmatrix}_{\eta_o}\begin{Bmatrix} C_{11} \\ C_{12} \\ C_{13} \end{Bmatrix}_{\eta_o} - \begin{Bmatrix} 0 \\ 0 \\ g \end{Bmatrix} = \begin{Bmatrix} 0 \\ 0 \\ 0 \end{Bmatrix} \tag{13}$$

The above equations reduce to the following constraints:

$$B_2 = B_3 = B_{11} = B_{21} = 0; \quad B_{31} = \frac{m_c}{\nu M_x} g \tag{14}$$

To compute the corresponding equilibrating currents, we note that the field and gradient at η_o is a linear function of currents in the five electromagnets [1] and are given by

$$B_i(x_o, \rho) = K_i \rho; \quad i = (1,2,3) \tag{15}$$

$$B_{ij}(x_o, \rho) = K_{ij} \rho; \quad i,j = (1,2,3) \tag{16}$$

where K_i and K_{ij} are 5 by 1 row vectors which denote the fields at x_o produced by each coil per unit of current. Thus the equilibrating currents, ρ_o, must satisfy the five linear equations

$$\begin{bmatrix} K_2 \\ K_3 \\ K_{11} \\ K_{21} \\ K_{31} \end{bmatrix} \rho_o = \begin{Bmatrix} 0 \\ 0 \\ 0 \\ 0 \\ \frac{m_c}{\nu M_x} g \end{Bmatrix} \tag{17}$$

which is identical to equation (54) in [1]. The 5 by 5 coefficient matrix turns out to be a well-conditioned full rank matrix and hence the equilibrating currents are unique and can be computed accurately. In summary, the current, ρ_o, which satisfies the latter equations, will generate a magnetic field that results in the equilibrium state, η_o.

2.3 Perturbed Motion About Equilibrium

Consider perturbed motion,

$$\rho = \rho_o + \delta\rho; \qquad \eta = \eta_o + \delta\eta \tag{18}$$

From the nonlinear equations, note that the roll rate of the cylinder, ω_1, is uncontrollable from the magnetic forces and the perturbed Euler parameter, $\delta\dot{\beta}_0$, equals zero at equilibrium, i.e., $\delta\beta_o$ is a constant. In addition, the variation in the Euler parameters is not independent since $\delta\dot{\beta}_1 = -\delta\dot{\beta}_2 - \delta\dot{\beta}_3$ from Eq.(1) and $\delta\dot{\beta}_0 = 0$. This means that three of the thirteen states can be eliminated in describing the perturbed motion as outlined below.

By defining the reduced (10 by 1) state vector

$$\xi = (\omega_2, \omega_3,\ \beta_2, \beta_3,\ v_1, v_2, v_3,\ x_1, x_2, x_3)^T \tag{19}$$

and using the second-order field approximation in Eq. (10) about the equilibrium, the linearized equation about η_o is given by

$$\delta\dot{\xi} = \hat{A}\delta\xi + \hat{B}\delta\rho + q_r \tag{20}$$

where $\delta\omega_1$ and $\delta\beta_0$ are constants, $\delta\beta_1 = -\delta\beta_2 - \delta\beta_3 - \delta\beta_0$,

$$q_r = \begin{pmatrix} \Gamma_2/I_c & \Gamma_3/I_c & O_{1\times2} & F_1/m_c & F_2/m_c & (F_3 + 2\nu M_x B_{31}\delta\beta_o)/m_c & O_{1\times3} \end{pmatrix}^T \tag{21}$$

and

$$\hat{A} = \begin{bmatrix} O_{2\times2} & -\frac{2\nu M_x}{I_c} B_1 I_{2\times2} & O_{2\times3} & \frac{\nu M_x}{I_c}\begin{bmatrix} -B_{31} & -B_{32} & -B_{33} \\ 0 & B_{22} & B_{23} \end{bmatrix} \\ \frac{1}{2} I_{2\times2} & O_{2\times2} & O_{2\times3} & O_{2\times3} \\ O_{3\times2} & \frac{2\nu M_x}{m_c}\begin{bmatrix} -B_{13} & 0 \\ -B_{23} & B_{22} \\ -B_{33} & B_{32} \end{bmatrix} & O_{3\times3} & \frac{\nu M_x}{m_c}\begin{bmatrix} B_{111} & B_{112} & B_{113} \\ B_{211} & B_{212} & B_{213} \\ B_{311} & B_{312} & B_{313} \end{bmatrix} \\ O_{3\times2} & O_{3\times2} & I_{3\times3} & O_{3\times3} \end{bmatrix} \tag{22}$$

$$\hat{B} = \nu M_x \begin{bmatrix} \frac{1}{I_c}\begin{bmatrix} -K_3 \\ K_2 \end{bmatrix} \\ O_{2\times 5} \\ \frac{1}{m_c}\begin{bmatrix} K_{11} \\ K_{21} \\ K_{31} \end{bmatrix} \\ O_{3\times 5} \end{bmatrix} \tag{23}$$

It can be shown that all ten states are completely controllable from the five coil currents. The open-loop system at the equilibrium state is also very unstable. For a detailed discussion of the physical significance of all modes, the interested reader is referred to [1].

2.4 Sensing and Actuation

Five physical variables are sensed indirectly and they are the pitch and yaw angles, and three displacements of the centroid. For large angles, the pitch and yaw angles (hence direction cosines) are related nonlinearly to the Euler parameters as given by Eq.(2).

For small angles, the rotation and displacements are actually perturbed rotations and displacements about the equilibrium state. The five physical variables sensed, denoted as y', are related approximately linearly to the Euler parameters as

$$y' = \begin{Bmatrix} \delta(\text{pitch}) \\ \delta(\text{yaw}) \\ \delta(\text{x-transl}) \\ \delta(\text{y-transl}) \\ \delta(\text{z-transl}) \end{Bmatrix} \approx \begin{Bmatrix} 2\delta\beta_2 \\ 2\delta\beta_3 \\ \delta x_1 \\ \delta x_2 \\ \delta x_3 \end{Bmatrix} = \hat{C}\delta\xi \tag{24}$$

where

$$\hat{C} = \begin{bmatrix} O_{2\times 2} & 2I_{2\times 2} & O_{2\times 3} & O_{2\times 3} \\ O_{3\times 2} & O_{3\times 2} & O_{3\times 3} & I_{3\times 3} \end{bmatrix} \tag{25}$$

In the laboratory, the actual measured outputs denoted by y are voltages and are related to the angular and translation variables and perturbed states by

$$y = [\text{p2s}]\ y' = [\text{p2s}]\hat{C}\delta\xi \tag{26}$$

Figure 2 shows the input and output block diagram of the LAMSTF plant. The input consists of five currents into five electromagnets and the measured outputs are five voltage signals. Very briefly, the current into the electromagnets generates a magnetic field which produces a net force and torque on the suspended cylinder, which is a permanent magnet. The resulting motion of the cylinder produces the pitch, yaw, and centroidal displacements that are sensed by a set of five optical shadow sensors that produce the output voltage signals. The sensor system has a high bandwidth and is modeled as an all-pass filter, i.e., the transfer function matrix is a constant, non-diagonal, non-singular matrix, denoted $[p2s]$.

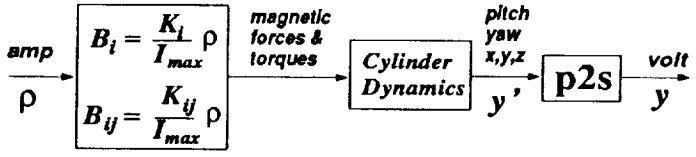

Figure 2: Block Diagram of LAMSTF Plant

3 Controller Design

3.1 Design Objectives

The main objective of the controller is to stabilize the cylinder and track a command signal about the equilibrium state. Of course the problem is complicated by the omni-presence of model errors and noise. Hence, robust tracking is sought. This requires the specification of a tracking performance index and the uncertainty set for which the tracking performance is supposedly guaranteed. While there are several ways to design multivariable stabilizing controllers, (for example, dissipative control, optimal linear regulator, eigensystem assignment, loop-at-a-time PID controller, or Youla parameterization), the challenging aspect is to guarantee a specific tracking performance in spite of imperfect knowledge of the actual physical system. Of course this guarantee is with respect to modeled uncertainty which itself may be uncertain. This in turn suggests that the designer's confidence level should be reflected in the degree of conservatism in the modeling of uncertainty, i.e., uncertainty in the uncertainty model itself is a real dilemma.

Controllers are sought for a set of plants that meet a certain tracking performance in contrast to optimizing the closed loop system for a particular plant. The set of plants is defined by the nominal and uncertainty models. The linearized analytical model derived from first principles is used as the nominal model while the perturbations are obtained from engineering judgement without the benefit of any system identification test data. Figure 3 illustrates the interconnection of the nominal plant, modeled uncertainties, and the controller structure. Besides the tracking command and performance loops, uncertainties at the

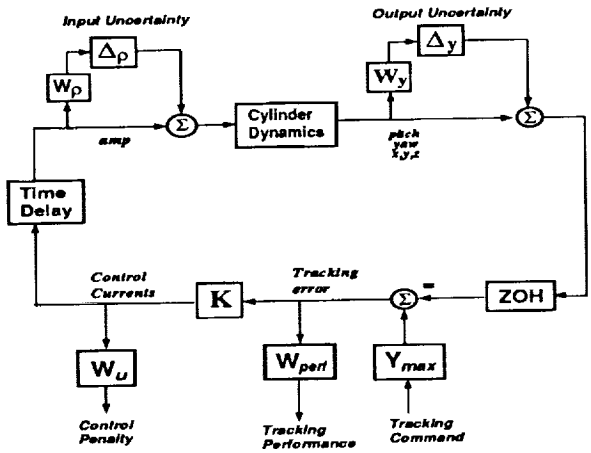

Figure 3: Interconnections of the LAMSTF system

plant input and output are included. The controller is also limited by a control penalty weight to prevent possible singular control solutions and to satisfy realistic actuator saturation constraints. Due to real time digital implementation, a computational time delay block and a zero-order-hold block are included. The following section provides details of the performance and uncertainty descriptions used in the control problem formulation.

3.2 Tracking Performance

The tracking performance of interest depends on the transfer functions from the tracking command, z_c, to the tracking error, e, where $e = z_c - y'$. This transfer function matrix is the sensitivity function matrix at the output and is written as

$$e/z_c = (I + GK)^{-1} \tag{27}$$

where GK denotes the loop gain matrix. In the sense of classical control, the inverse return difference (or sensitivity matrix) should be made small or alternately, the loop gain should be large over a bandwidth,

BW_{track}, of interest where tracking performance is desired. In terms of multivariable control, this requirement for smallness of the inverse return difference matrix can be defined by principal gains (i.e., singular values of transfer matrices) such that

$$\bar{\sigma}\left[(I+GK)^{-1}\right] \leq p(j\omega); \quad \forall\omega \in [0,\infty) \tag{28}$$

where the performance weighting function, $p(j\omega)$, which is chosen as a rational polynomial, should be relatively small over the bandwidth, BW_{track}.

So far, the above requirements assign equal importance to each component of the vector of error signals. However, two factors should further influence the tracking performance metric, namely, differing units and range of signals, and relative physical importance of signals. For this control design for LAMSTF, it is assumed that the maximum amplitudes of the desired tracking command are given by

$$Y_{max} = \text{diag}\left(\pm\tfrac{\pi}{180}rad \quad \pm\tfrac{\pi}{180}rad \quad \pm.0005meters \quad \pm.0005meters \quad \pm.0005meters \right) \tag{29}$$

By normalizing the tracking command input by the absolute values of the above matrix, the command input will be normalized to unity. Note that the maximum singular value corresponding to this scaled transfer function from command input to tracking error can be interpreted as the maximum 2-norm error with respect to all unit 2-norm bounded tracking command vectors, scaled by Y_{max}. The tracking errors are then normalized by Y_{max}^{-1} to account for differing units and range of signals. Furthermore, the relative physical importance of the error signals are defined by a constant diagonal matrix, Φ, where $\Phi = \text{diag}(.9, .5, .5, .3, .3)$. The above requirements can be summarized as

$$\bar{\sigma}\left[\Phi Y_{max}^{-1}(I+GK)^{-1}Y_{max}\right] \leq p(j\omega); \quad \forall\omega \in [0,\infty) \tag{30}$$

In terms of H_∞ norm the above weighted constraint on the inverse return difference transfer function matrix becomes

$$\|W_{perf}(I+GK)^{-1}Y_{max}\|_\infty \leq 1 \tag{31}$$

where $W_{perf} = p(s)^{-1}\Phi Y_{max}^{-1}$.

Figure 4 shows the performance weight, $p(j\omega)$, used in the design. The first-order polynomial

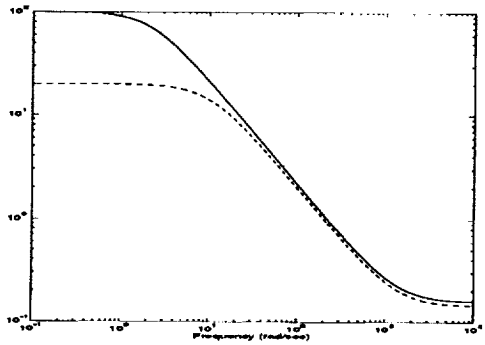

Figure 4: Frequency Weights $p(s)^{-1}$ for Tracking Performance. Performance case (solid), Robust case (dashed)

$$p(s) = f_{DC}\left[\frac{(s+\omega_n)}{(s+\omega_d)}\left(\frac{\omega_d}{\omega_n}\right)\right] \tag{32}$$

was chosen with $\omega_n = 2.2$ r/s, $\omega_d = 1400$ r/s, and $f_{DC} = .01$ for the performance case and $\omega_n = 10$ r/s, $\omega_d = 1400$ r/s, and $f_{DC} = .05$ for the robust case. This weight specifies the steady state tracking error to be within 1 % for the performance case, and within 5 % for the robust case. The weight decreases by 20 db per decade until 1400 rad/s. This frequency weighting results in the tracking error reaching 100% at a frequency of about 200 rad/s for both controllers. The slightly higher bandwidth for the performance case will yield a controller with a slightly faster rise time. Note that this weighting is suited for step commands which have similar slope. In the sequel, the performance parameters are varied to tradeoff with robustness.

3.3 Model Uncertainty and Noise

3.3.1 Uncertainties at Input

There are several causes for model uncertainties in the LAMSTF system. An important source of error, which is difficult to model, is the implicit error in the linearized model about the assumed equilibrium state. Because of unquantified uncertainties in the constants assumed for the second-order (first order for field gradients) magnetic field model, the true magnetic field produced by the five electromagnets may deviate from the predicted values. Since the true values for the equilibrium currents (and hence the correct linearized model) would require the precise knowledge of the magnetic field and its gradients as given by Equation (17), these errors affect both the equilibrating and stabilizing magnetic fields.

This error affects the values for the nominal plant $\delta\hat{A}$ and $\delta\hat{B}$. It can be shown through a perturbation analysis about equilibrium that inexact magnetic field values (parameter errors) and corresponding equilibrium current errors will appear as constant forcing terms in the linear state equations. These linearization errors are approximately modeled as uncertainties in the equilibrating currents, i.e., at the input of the plant.

Other sources of uncertainties include calibration errors, temperature effects, electrical noise and bias error in the current signal that produces the magnetic field. All of the above factors are lumped together and modeled as bounded multiplicative uncertainties at the input.

The uncertainties at the inputs are taken as $\Delta_\rho W_\rho$ where Δ_ρ are arbitrary unstructured matrices that satisfy

$$\|\Delta(s)_{curr}\|_\infty \leq 1; \tag{33}$$

and $W_\rho = f_\rho I_{5\times 5}$.

Figure 5 shows the maximum multiplicative uncertainty assumed at the plant input. While the

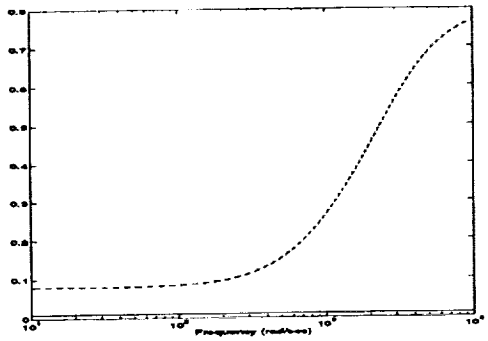

Figure 5: Frequency Weighting for Input Uncertainty. Performance case (solid), Robust case (dashed).

uncertainty for the performance case assumes only 1% error, the uncertainties in all five actuating current signals into the coils for the robust case is assumed to have 8% error at low frequencies and rolls up linearly at 300 rad/sec to attain values of more than 30% error at 1250 rad/sec (200 Hz). The uncertainties are assumed fully coupled, i.e., unstructured.

3.3.2 Uncertainties at Output

The sensing system provides measurements of the pitch and yaw angles and the location of the centroid. It consists of five shadow sensors which detect the amount of unblocked light passing the suspended element. The light is detected by photodetectors, converted to voltage signals, and transformed to provide the five position and orientation parameters. There are various limitations to performance of this system, including noise, calibration errors, and dynamic range.

The noise is expected to be larger at higher frequencies and control activity should be limited accordingly. The calibration errors cause inaccurate gains and may lead to spurious coupling between the different degrees of freedom. Also of importance is the linear range of the sensors which are limited to $\pm 1^o$ for pitch and yaw

and .5 millimeters for x,y, and z axes. Any motion beyond the above ranges results in high non-linearity and/or sensor saturation.

To approximately model the above uncertainties, an unstructured frequency dependent multiplicative uncertainty at the plant output of the following form is proposed:

$$p_y(s) = f_y \left[\frac{(s+\omega_n)}{(s+\omega_d)} \left(\frac{\omega_d}{\omega_n} \right) \right] \tag{34}$$

with parameters, $\omega_n = 180$ r/s, $\omega_d = 1800$ r/s, and $f_y = .06$. While the output uncertainty for the performance case was chosen at 1% constant over all frequencies, the weight parameters for the robust case specify the maximum uncertainty in the sensor signal at low frequencies to be 6 % and increase, as shown in Figure (6), to 60 % at 1800 rad/sec to provide noise immunity (see Fig. 6).

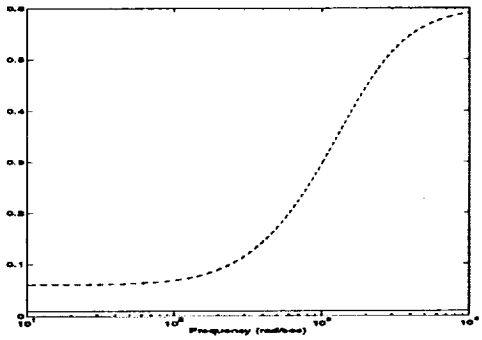

Figure 6: Frequency Weighting for Output Uncertainty. Performance case (solid), Robust case (dashed).

The above uncertainties were chosen for the pitch, yaw, and x,y,z outputs which have different units. Hence, as was done with the inputs, the outputs are initially normalized and then finally de-normalized to account for different units in the unstructured uncertainties. Figure 7 shows the output weighting procedure in block diagram form.

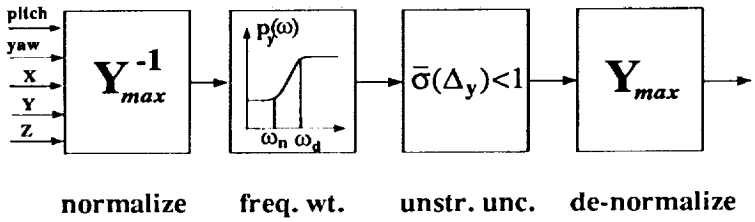

Figure 7: Output Uncertainty Weighting.

3.4 Controller Weights, Time Delay, and Zero-Order-Hold

In the implementation of controllers, the importance of various practical constraints besides signal noise becomes evident. First, the outputs of the actuators are limited by the saturation amplitude of the input currents. Figure 8 shows the frequency weighting of the control effort in all five channels. The DC gains are used for penalizing excessive control power while the increase in the penalty at higher frequency is used to encourage controller roll-off. The actuator electromagnets have sufficient bandwidth to behave as all-pass filters and hence are approximated by constants with saturation limits.

All controllers were designed assuming a continuous system but were implemented digitally. The use of real-time digital computers means that the analog signals must be discretized by sampling followed by zero-order-hold, with the further complication of a computational delay. The above discretization effects are

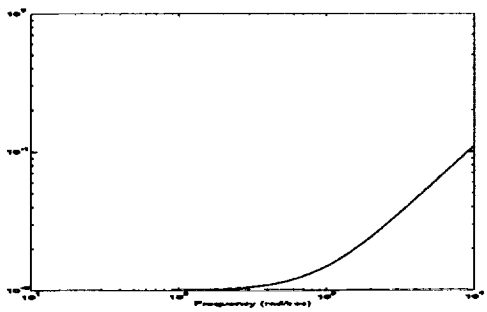

Figure 8: Controller Penalty Weighting

approximately accounted for in the continuous control design by introducing continuous approximations of a pure time delay and a zero-order-hold as shown below:

$$\Delta T = e^{-sT} \approx \frac{1 - \frac{sT}{2}}{1 + \frac{sT}{2}} \qquad ZOH = \frac{1 - e^{-sT}}{sT} \approx \frac{1 - \frac{sT}{6}}{1 + \frac{sT}{3}} \tag{35}$$

A pure time delay of $\frac{1}{5}$ sampling period was assumed. It was discovered that compensators designed without the inclusion of these effects had poor performance when implemented digitally, due to significant phase errors occurring at high frequencies.

A small amount of pure time delay is implicitly accommodated for by the input and output multiplicative uncertainty used because the uncertainty is modeled as complex quantities bounded only by their norms. However, the phase delay accommodated is only about 5.7 degrees for an assumed uncertainty of 10 percent and is equal for all frequencies.

3.5 μ Analysis/Synthesis

The benefit of the μ-analysis and synthesis framework is that performance robustness for a fairly general class of robust control problems can be precisely defined by the scalar, μ. The underlying theory which forms the basis of this method is discussed in detail in [8]-[11]. Currently, μ cannot be computed directly for a general structure. Instead, an upper bound is computed for both analysis and synthesis purposes. Lower bounds are computed mainly to evaluate the degree of conservatism of the upper bound. Designing controllers by μ synthesis involves an iterative minimization of the upper bound using H_∞ methods. The μ-design problem is summarized as follows:

$$\begin{array}{ll} \text{minimize} & \|DF_l(P,K)D^{-1}\|_\infty \\ F_l(P,K) \in H_\infty, & D \in \underline{D} \end{array} \tag{36}$$

where the set of scaling matrices, $\underline{D}$, has a similar structure as $\underline{\Delta}$ (the structured uncertainty matrix) with an appended identity matrix. The terms, F_l, P, and K, denote the lower linear fractional transformation, augmented plant, and the controller, respectively.

For the LAMSTF problem, Figure 9 shows the augmented plant, P which includes the performance and uncertainty weights.

Figure 10(a) shows the actual uncertainty and the controller connections so that robust performance can be evaluated via μ-analysis. This involves the numerical evaluation of μ which is approximated by the lower and upper bounds. The analysis could include the evaluation of the degree to which robust stability and nominal performance are satisfied independently hence providing valuable hints on a possible tradeoff. The level and shape of μ achieved usually indicates a need for improvement in the controller.

Having decided that the controller needs refinement, an approach to improving μ is called the "D-K iteration". In this approach, K or D is optimized independently and sequentially; by fixing D, K is obtained from a scaled H_∞ optimization problem and, by fixing K, a convex optimization is performed at

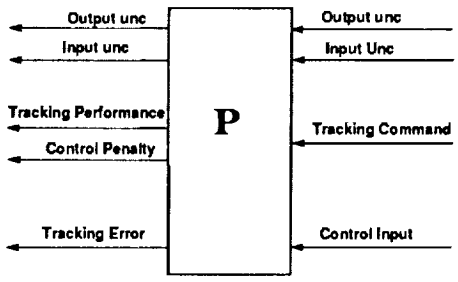

Figure 9: Augmented Plant of LAMSTF

each frequency with respect to $ln(D)$. Note that optimizing for D while keeping K fixed involves the search for the minimal upper bound on μ while optimizing for K while fixing D involves the minimization of an approximation of μ itself. Figure 10(b) shows the closed loop transfer function of interest, $F_l(P, K)$, and the scaling matrix, D which form the scaled H_∞ problem. Although this approach is iterative in nature and

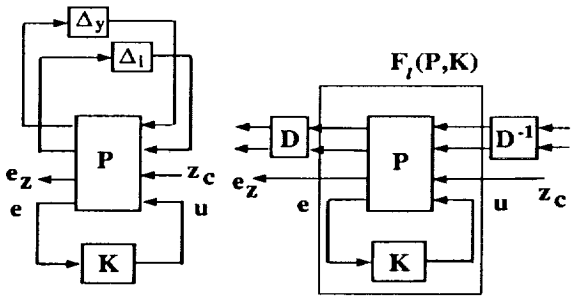

Figure 10: (a) Robust Performance; (b) μ-synthesis

convergence to a global minimum is not guaranteed, past numerical studies show excellent convergence. For example, in the recent robust line-of-sight control problem [6], typically 2 or 3 iterations were sufficient. In this study, 2 iterations are made. To solve the H_∞ problem the Glover-Doyle algorithm [9] is used. The MATLAB toolbox, μ-Tools [12] is used in this study for the analysis and synthesis of the controllers.

3.6 Control Designs

Four controllers are designed and analyzed in the following: performance H_∞, performance μ, robust H_∞, and robust μ. In computing the structured singular values, all controllers were reduced to 30 states by internal balancing. The controllers were reduced to ease computational burden, since many of the states were very weakly controllable and observable.

For the performance case, the H_∞ and μ controllers gave H_∞ norms of 1.75 and 1.18 and from Figure 11, μ values of 1.27 and 1.18 respectively (although the upper bound for perf MU case from the figure is larger, μ must be less than the corresponding H_∞ norm). Therefore, although the H_∞ norms are significantly different, robust performance is similar from the μ plots. This is expected for the performance case where the uncertainty levels specified are small. Note also that the upper and lower bounds of μ for both cases are close which is consistent with past experience.

For the robust case, the H_∞ and μ controllers gave H_∞ norms of 3.81 and 1.70 and from Figure 12, μ values of 2.75 and 1.70 respectively. The significant decrease in μ for the robust μ case over the robust H_∞ case means that a significant robust performance improvement is expected. This is expected for the robust case where the uncertainty levels specified are not small. Basically, due to the larger uncertainties specified, the H_∞ design produces very conservative results because performance and robustness constraints cannot be satisfactorily incorporated without using structured singular values. The peak of the μ plots for the robust HINF case also shows that it is difficult to satisfy robust performance due to the highly unstable

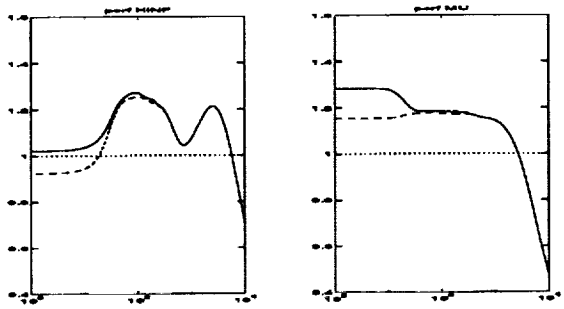

Figure 11: μ upper and lower bounds for Perf HINF (left) and Perf MU (right).

pitch and yaw modes at approximately 60 rad/sec [1]. The μ plots also indicate that tracking performance under significant uncertainty at low frequencies drives the design problem for both H_∞ and μ controllers. Again note that the upper and lower bounds of μ for both cases are close which is consistent with past experience. Note that the initial peaks are flattened for the μ controller indicating near optimal conditions.

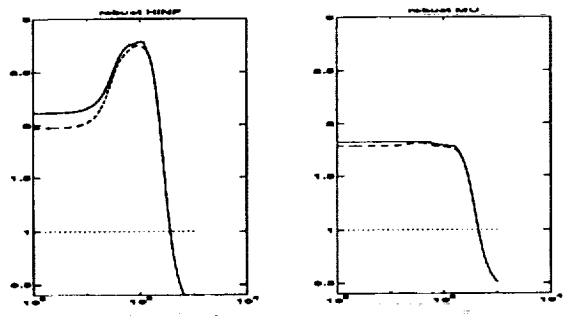

Figure 12: μ upper and lower bounds for Robust HINF (left) and Robust MU (right).

The previous plots show μ values for differing sets of constraints. For comparison purposes (perf case vs. robust case), the constraint weightings for the robust controllers were used for computing μ for all controllers. Figure 13 shows the near converged μ plots for H_∞ and μ controllers for performance and robust cases. Each plot shows robust performance (top line), nominal performance (middle) and robust stability (bottom). Note that at low frequencies, the performance controller is better while the robust controller is better at higher frequencies. It is also clear that the performance MU controller is not much better than performance HINF controller. However, robust MU controller is expected to perform better at lower frequency (i.e. tracking) while slightly worse at higher frequencies than robust HINF controller. Interestingly, in all cases, robust stability is easily satisfied even for the performance controllers. We note that the μ (peak) of performance μ controller is slightly smaller than the robust μ controller. This is probably due to factors such as suboptimality in the H_∞ and D-K iterations and model reduction errors.

In summary, the μ design did not improve over the H_∞ design for the performance case but is significantly better for the robust case. The performance controller is expected to perform better at lower frequencies where tracking occurs while the robust controller is expected to perform better at higher frequencies. These analytical predictions were tested in laboratory and are discussed in the next section.

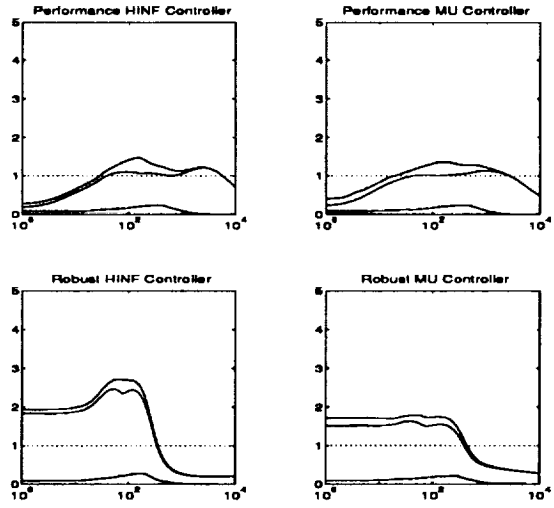

Figure 13: μ: upper bounds for robust perf, nominal perf, and robust stab

4 Results

4.1 Controllers Tested and Model Reduction

Speed limitations of the real time control computer required that the 30 state controllers be implemented at a sample rate of about 600 Hz. The four controllers had loop-gain bandwidth of about 110 Hz, and it was discovered that discretizing at this speed was inadequate. Therefore, further model reduction, through balanced realization, was performed and the controllers were implemented with fewer states at higher sampling rates. For the performance controllers 20 states were implemented at 800 Hz, while for the robust controller, which had a slightly larger bandwidth, 17 states were implemented at 850 Hz. The

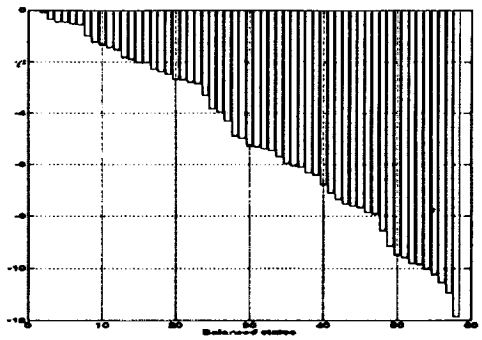

Figure 14: Normalized Hankel SV for Robust MU controller

normalized truncation error is shown in Fig. 14 for the robust MU controller case. For 30 states, the singular value error is less than 10^{-5} while for 17 states, the error is nearly 10^{-2}, i.e., the least significant normalized singular value increased by 3 orders of magnitude for the reduced models. A reasonably reduced controller is expected to be approximately the size of the augmented plant, which was 30. Therefore, for the highly reduced compensators which were implemented the robustness properties of the controllers must be reevaluated and these properties considered when interpreting the experimental results.

The μ values were recomputed for the 17 states and 20 states controllers which were actually imple-

mented. Figure 15 shows a significant decrease in robust performance predicted by reducing from 30 to 20 states for performance case and by reducing 30 states to 17 states for the robust case. Note that for the H_∞ cases, even robust stability (bottom lines) is not satisfied (cf. Figure 13). Therefore, the actual controllers implemented are not expected to perform as well for a reasonable sampling rate.

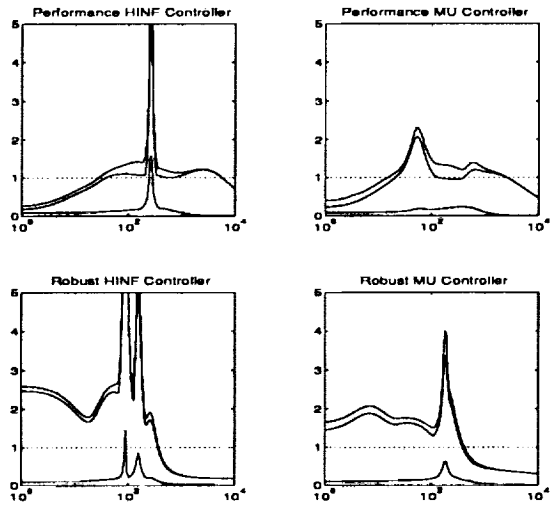

Figure 15: μ upper and lower bounds for reduced order Perf HINF (left) and Perf MU (right).

4.2 Comparison of Simulation and Experiment

Figure 16 shows the differences between simulation and experiments for the robust H_∞ and μ controllers. Each pair of plots shows a step tracking response in a particular axis and the total control power required to produce the response. The simulation involved an analog plant controlled by a discrete controller of the same order which was implemented. The simulation included a pure time computational delay of 4.3×10^{-4} seconds.

The figures show that the simulation is close to experimental results for the translational motions. The rise time and steady state values are fairly close in all cases. The damping however is quite different, especially in pitch and yaw. The power used in the test is quite similar to the predicted values except at later times where residual motions exist only in the experiments. Note that the experimental responses for the robust H_∞ design (Fig. 16) show large oscillations which are at approximately 20 Hz which are not apparent in the simulation. This discrepancy is consistent with the μ plots in Figure 15 where the μ peaks occur at approximately the same frequencies.

Figure 17 shows the simulation versus experimental comparison for the performance controllers. The responses are closer to simulation for these cases than for the robust design; however, they exhibit the same type of damping errors in the pitch and yaw tracking response.

4.3 H_∞ versus μ

Figure 18 shows the experimental comparisons between H_∞ and μ controllers for both performance and robust cases. The μ controller is only slightly better than H_∞ controller for the performance case. This is consistent with the fact that the μ values for both the robust and performance cases, as shown in Figure 13, are similar. However, the μ controller is significantly better than H_∞ controller for the robust case. Again, this is consistent with the significantly different μ values for the robust and performance cases, as shown in Figure 13. Notice that the μ controller generally requires less control power but gives better performance than H_∞ controller. Note also that the power levels are larger for tracking rotational degrees of

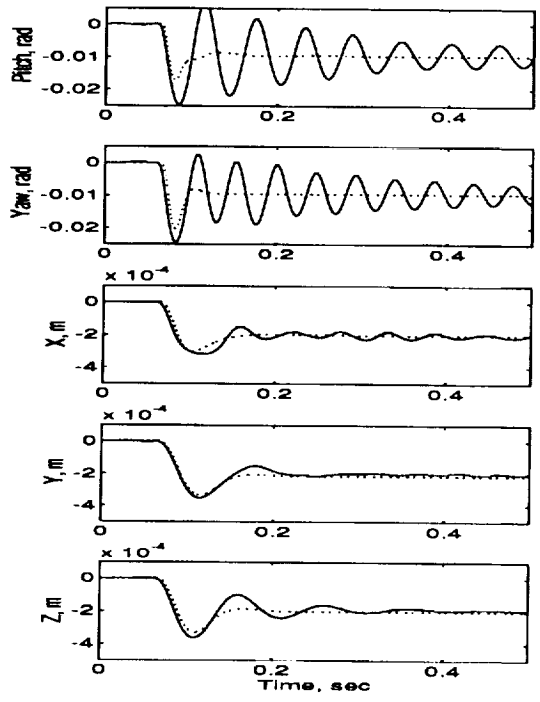

(a) Position, H_∞

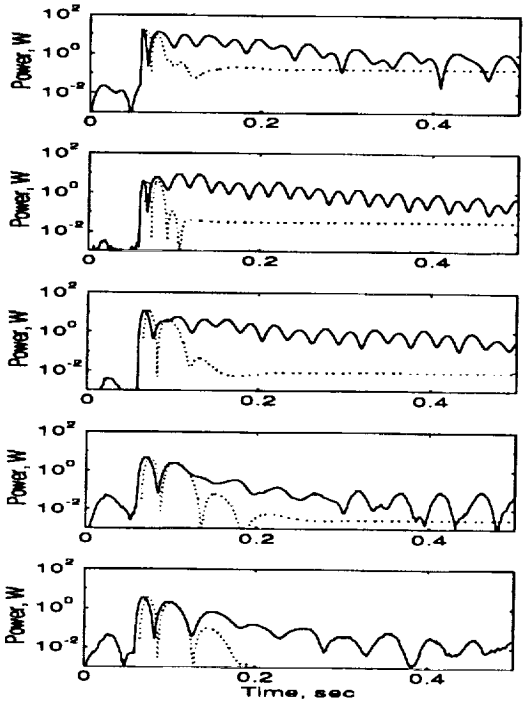

(b) Control Power, H_∞

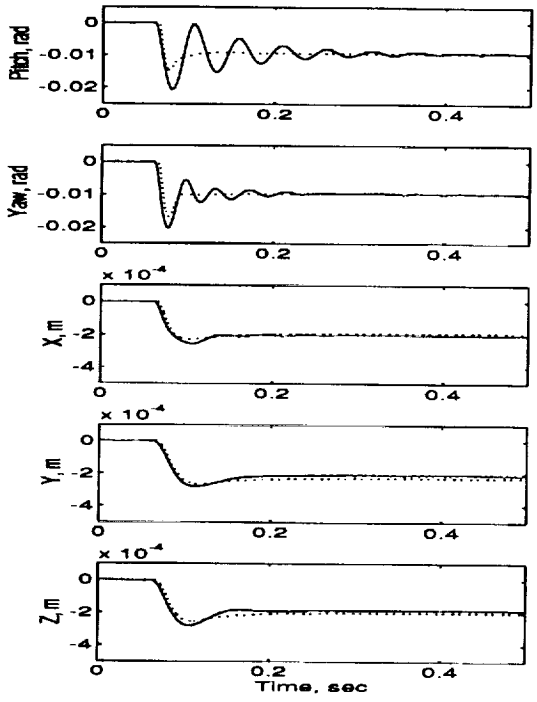

(a) Position, μ

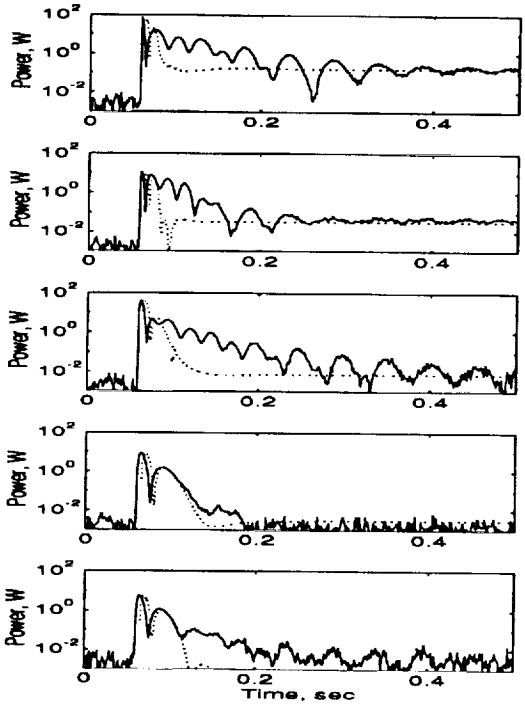

(b) Control Power, μ

Figure 16: Experiment (solid) vs Simulation (dotted), Robust designs

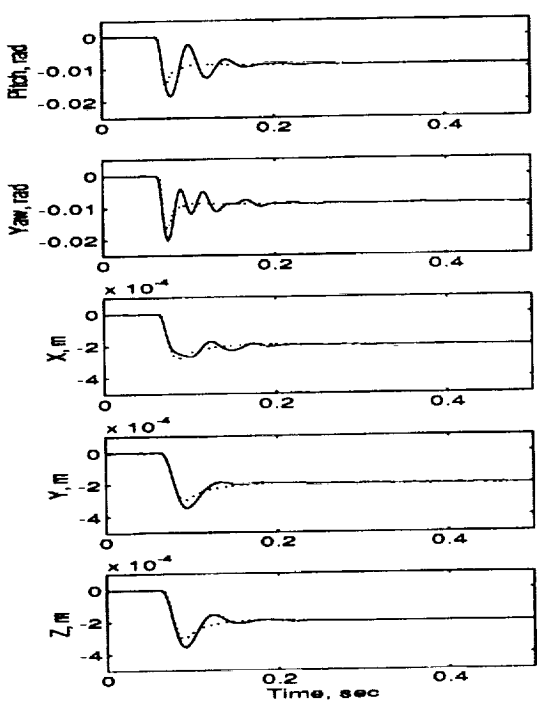

(a) Position, H_∞

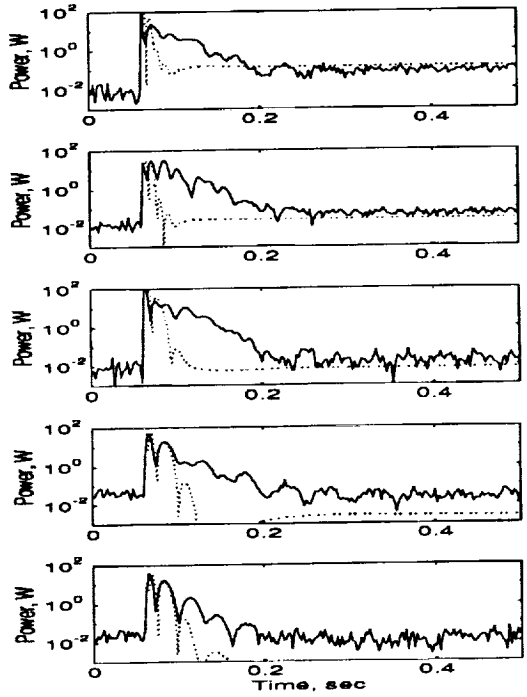

(b) Control Power, H_∞

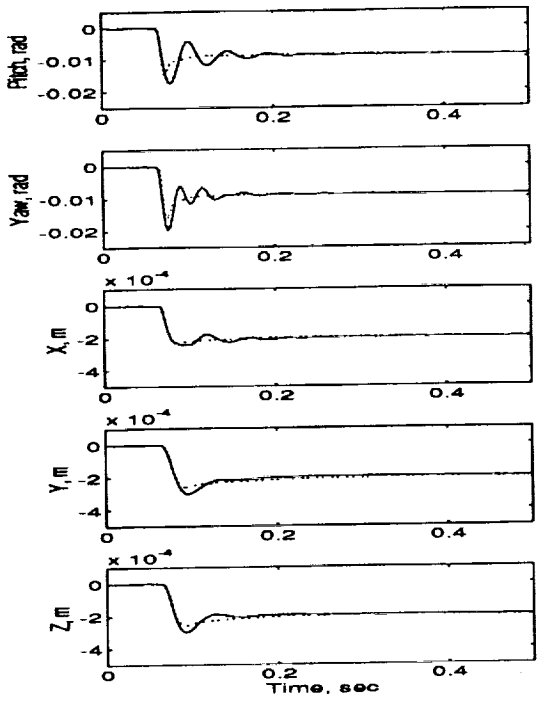

(a) Position, μ

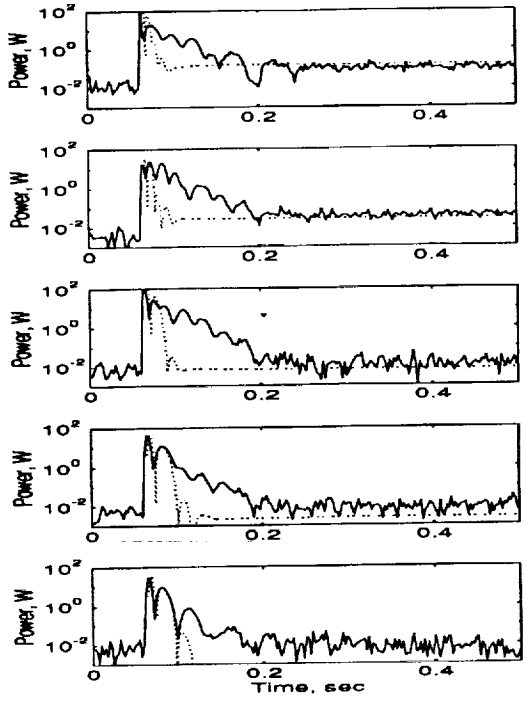

(b) Control Power, μ

Figure 17: Experiment (solid) vs Simulation (dotted), Performance designs

freedom. This is expected because the rotational modes, which have real poles near +60 rad/s, are violently unstable and at a higher frequency than the translational modes.

4.4 Performance and Robustness Tradeoffs

Figure 19 shows the experimental comparison between controllers designed for performance with small uncertainties versus controllers designed for performance with significant levels of modeled uncertainties. Figure 19 shows that the performance H_∞ controller has significantly better tracking response than the robust H_∞ controller. While it is clear that the performance controller gives significantly better tracking response than the robust controller for the H_∞ designs, for the μ designs the performance and robust controllers were more nearly matched. Unfortunately, the H_∞ is not able to handle the inclusion of significant levels of uncertainties along with the tracking performance constraints, and a low overall robust tracking performance is obtained in the laboratory.

4.5 Robust Tracking under Measurement Noise

To investigate the effect of external high frequency noise on the closed loop stability and tracking performance, colored Gaussian noise was introduced at the input to the controller. A large noise level was chosen to highlight its effects on the closed loop response. Figure 20 shows the frequency spectra of experimental response of the performance and robust cases for H_∞ controllers. The figures show improved noise rejection of up to a frequency of 300 and 200 Hz for rotational and translation axes respectively. At the lower frequencies, the robust case reduces the noise response by approximately 20 decibels. Note that the improved noise rejection properties of the robust case are anticipated from output uncertainty weighting shown in Figure 6 and the μ plots of Figure 15. Figure 21 shows experimental tracking response of y-axis under severe noise for performance and robust H_∞ controllers. Notice that the step in the tracking command input is almost lost in the noise. The other degrees of freedom also had similar noise added to their signals. The tracking response for the robust case is significantly better than the performance controller and it is very similar to the noiseless responses obtained previously.

5 Concluding Remarks

The purpose of the experiments was to address what-if questions on common models of uncertainties and was not explictly taylored for the LAMSTF testbed. The structure and the level of uncertainties assumed are only roughly known, without the benefit of any system identification results and are modeled as simple multiplicative uncertainties at the plant inputs and outputs. No attempt has been made to refine the nominal and uncertainty models through testing. Not surprisingly, comparisons between experiments and simulation indicate that the uncertainty model assumed is itself significantly inaccurate, especially in the rotational modes. Further robust system identification experiments aimed at improving the nominal and uncertainty models are needed for further improvement in robust performance. It is noted that the LAMSTF is highly open loop unstable. This means that some form of closed loop system identification can only be applied, which significantly complicates the problem of improving uncertainty models through experimental data.

In spite of the uncertainty in the uncertainties assumed, the experimental results confirmed the following simulation/design predictions: (i) μ design did not improve over the H_∞ design for the performance case but was significantly better for the robust case, (ii) performance controllers gave better tracking performance than robust controllers at lower frequencies, and (iii) robust controllers gave better tracking performance under high measurement noise levels. Analytical and experimental results indicate that a satisfactory level of robust tracking can be achieved for the highly unstable LAMSTF system. The speed of the real time controller significantly limited the implementation of modern multivariable robust controllers and further improvement is suggested. From a testbed standpoint, this study demonstrates analytically and experimentally that when significant uncertainties must be included in a control system, optimizing μ can be quite useful over direct H_∞ design.

Although nothing concrete has been proven, the results of this study provide a better understanding and appreciation of the physical significance of the numerous weighting parameters often encountered by the

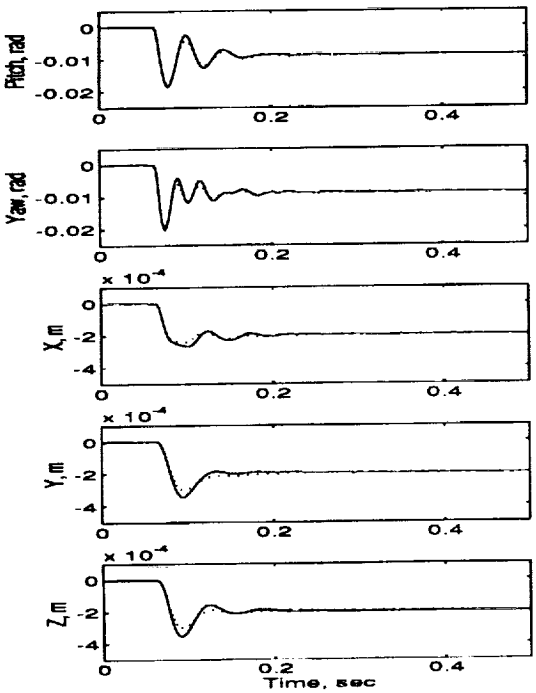

(a) Position, Perf Controller

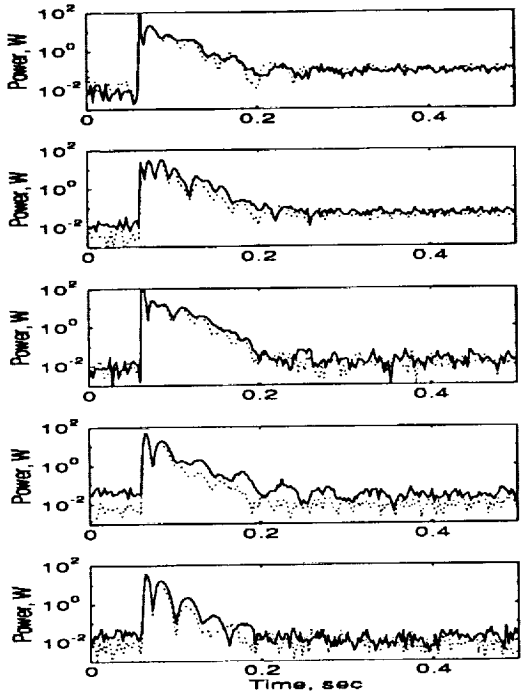

(b) Control Power, Perf Controller

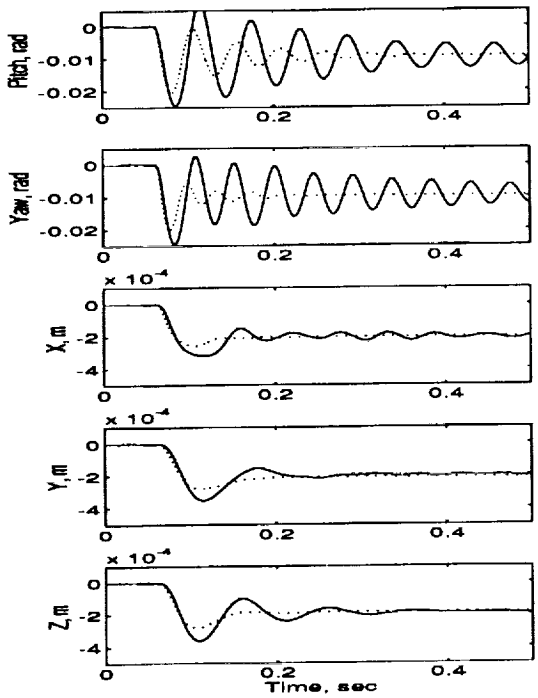

(c) Position, Robust Controller

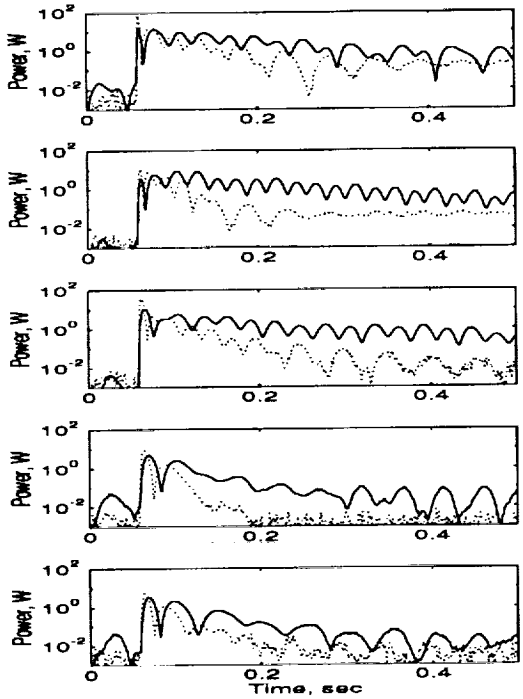

(d) Control Power, Robust Controller

Figure 18: Experimental comparison, H_∞ (solid) vs μ (dotted).

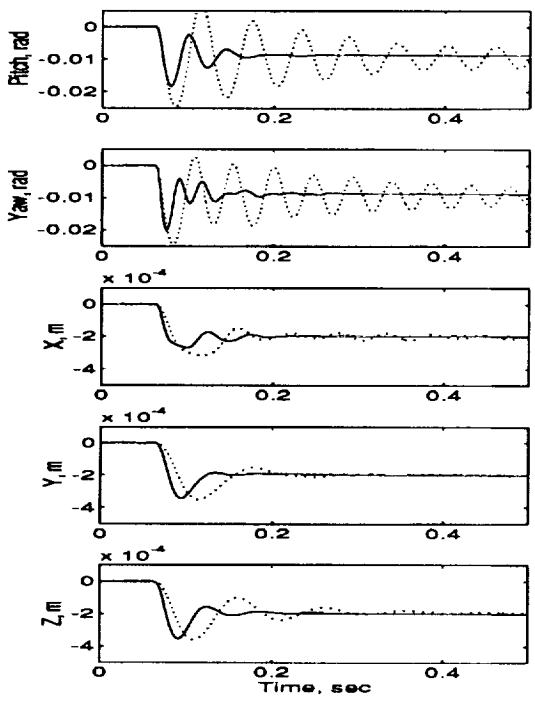

(a) Position, H_∞

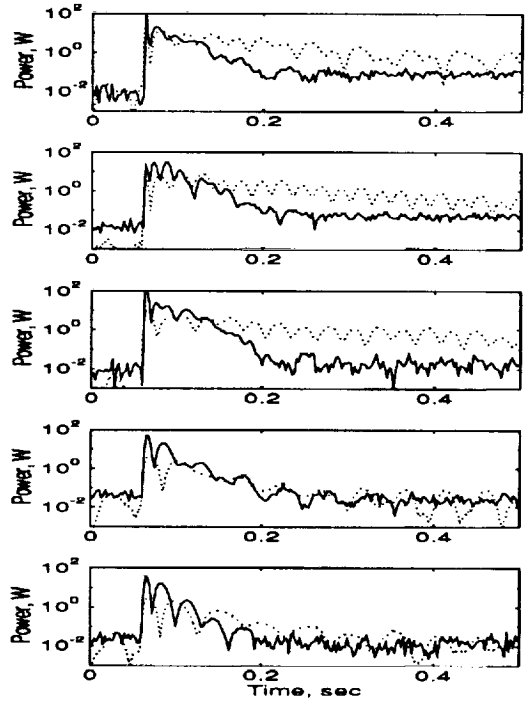

(b) Control Power, H_∞

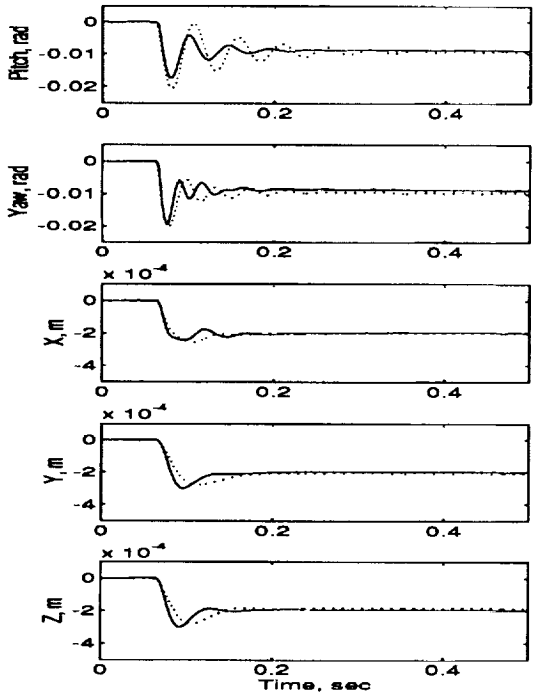

(a) Position, μ

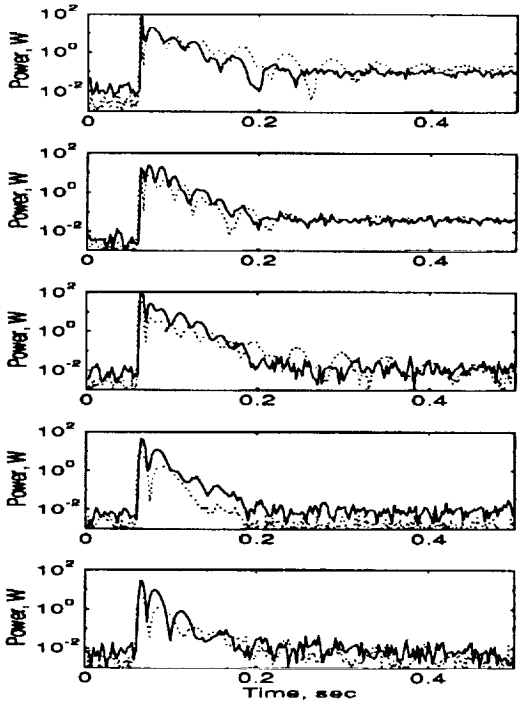

(b) Control Power, μ

Figure 19: Performance (solid) vs Robustness (dotted).

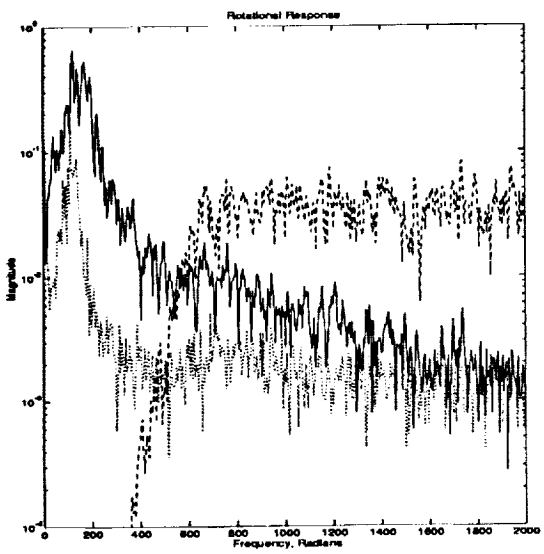

(a) Rotation

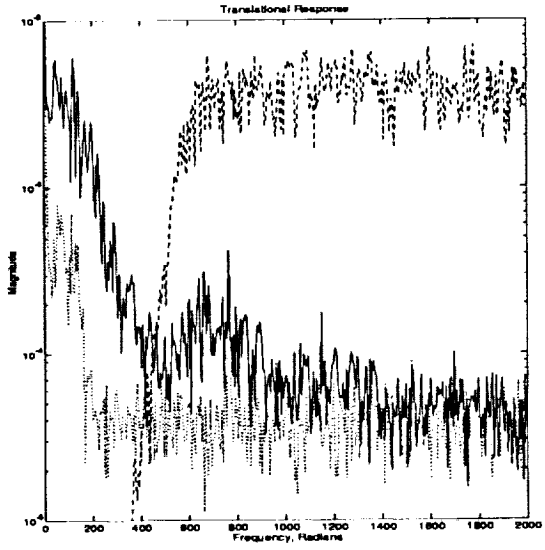

(b) Translation

Figure 20: Frequency spectra of experimental response with high frequency noise input. Performance (Solid), Robust (Dotted), Input (Dashed).

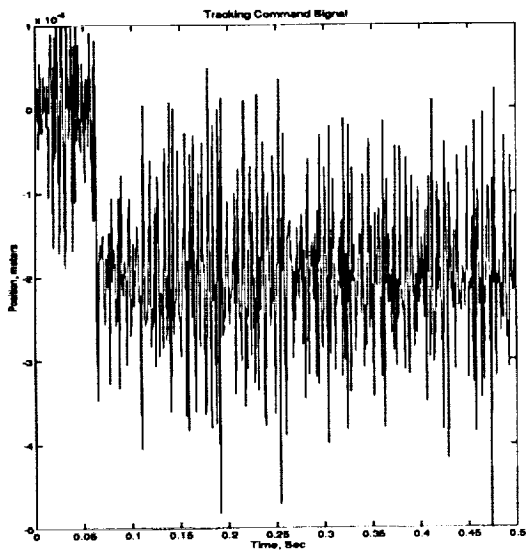

(a) Command input

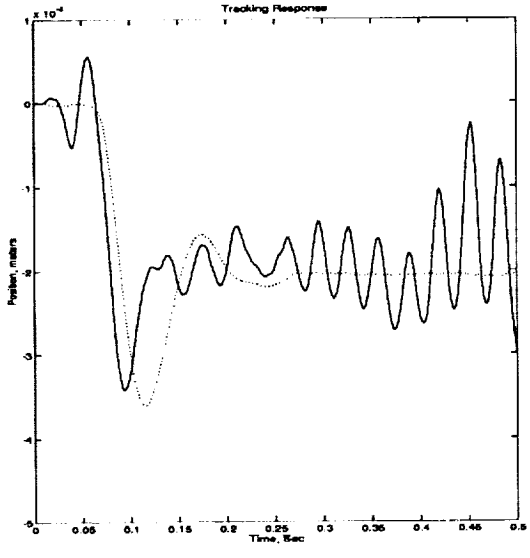

(b) Tracking response

Figure 21: H_∞ Controller tracking with noisy input. Performance (Solid), Robust (Dotted).

control designer in the application of H_∞ based control design techniques. In this regard, this study has been quite useful.

6 Acknowledgements

The authors would like to thank Mr. Nelson J. Groom and Mr. Tom Britton for their helpful comments in the investigation of control laws for LAMSTF system.

References

[1] Groom, N.J., and Britcher, C.P., "Open-Loop Characteristics of Magnetic Suspension Systems Using Electromagnets Mounted in a Planar Array," NASA-TP 3229, November 1992.

[2] Balas, G.J., and Doyle, J.C., "Robust Control of Flexible Modes in the Controller Crossover Region," *American Control Conference*, Pittsburg, PA, June 1989.

[3] Balas, G.J., and Doyle, J.C., "Robustness and Performance Tradeoffs in Control Design for Flexible Structures," *29-th IEEE CDC*, Hawaii, December 1990.

[4] Balas, G.J., and Lim, K.B., "Control of a Flexible Structure in the Presence of Natural Frequency Uncertainty with H_2 Performance Specifications," *American Control Conference*, San Francisco, CA, June 1993.

[5] Lim, K.B., Maghami, P.G., and Joshi, S.M., "A Comparison of Controller Designs for an Experimental Flexible Structure," *IEEE Control System Magazine*, Vol.12, No.3, June 1992.

[6] Lim, K.B., and Balas, G.J., "Line-of-Sight Control of the CSI Evolutionary Model: μ Control," *American Control Conference*, Boston, MA, June 1992.

[7] Junkins, J.L., and Turner, J.D., *Optimal Spacecraft Rotational Maneuvers*, Elsevier Science Publishers, New York, 1986.

[8] Doyle, J.C., "Analysis of Feedback Systems with Structured Uncertainties," Proc. IEE-D 129, 1982, pp. 242-250.

[9] Glover, K. and Doyle, J.C., "State-Space Formulae for all Stabilizing Controllers that Satisfy an H_∞ Norm Bound and Relations to Risk Sensitivity," *Systems and Control Letters*, vol. 11, pp. 167-172, 1988.

[10] Doyle, J.C., Glover, K., Khargonekar, P., and Francis, B., "State-Space Solutions to Standard H_2 and H_∞ Control Problems," *IEEE Transactions on Automatic Control*, Vol.34, No.8, August 1989.

[11] *MUSYN Robust Control Short Course Lecture Notes*, Arcadia, CA, September, 1989.

[12] Balas, G.J., Doyle, J. D., Glover, K., Packard, A. K., and Smith, R., *μ-Analysis and Synthesis Toolbox*, MUSYN Inc., Minneapolis, 1991.

OMIT

Session 10b – Superconducting Suspensions

Chairman: Willard W. Anderson
NASA Langley Research Center